TU Delft

Delft University of Technology

Document Version
Final published version

Licence
Dutch Copyright Act (Article 25fa)

Citation (APA)
Atmaca, D., de Visser, C., & van Kampen, E.-J. (2026). Active Incremental Nonlinear Dynamic Inversion for Sensor and Actuator Fault-Tolerant Control. *Journal of Guidance, Control, and Dynamics*, *49*(7), 2180-2190. https://doi.org/10.2514/1.G009705

Important note
To cite this publication, please use the final published version (if applicable).
Please check the document version above.

Copyright
In case the licence states “Dutch Copyright Act (Article 25fa)”, this publication was made available Green Open Access via the TU Delft Institutional Repository pursuant to Dutch Copyright Act (Article 25fa, the Taverne amendment). This provision does not affect copyright ownership.
Unless copyright is transferred by contract or statute, it remains with the copyright holder.

Sharing and reuse
Other than for strictly personal use, it is not permitted to download, forward or distribute the text or part of it, without the consent of the author(s) and/or copyright holder(s), unless the work is under an open content license such as Creative Commons.

Takedown policy
Please contact us and provide details if you believe this document breaches copyrights.
We will remove access to the work immediately and investigate your claim.

This work is downloaded from Delft University of Technology.

JOURNAL OF GUIDANCE, CONTROL, AND DYNAMICS
Vol. 49, No. 7, July 2026

Technical Notes

Active Incremental Nonlinear Dynamic Inversion for Sensor and Actuator Fault-Tolerant Control

Direnc Atmaca,* Coen de Visser,† and Erik-Jan van Kampen‡
Delft University of Technology, 2629 HS Delft, The Netherlands

https://doi.org/10.2514/1.G009705

Downloaded by Technische Universiteit Delft on July 21, 2026 | http://arc.aiaa.org | DOI: 10.2514/1.G009705

I. Introduction

AIRCRAFT today rely extensively on a broad range of sensors and actuators for flight control. Simultaneous failures of these systems threaten flight safety, especially in turbulent flight conditions. As a result, addressing these faults represents an important problem in flight control.

Incremental nonlinear dynamic inversion (INDI) is a control method similar to feedback linearization that relies on both model and sensor information [1]. To derive a linearizing law, INDI requires an onboard control effectiveness model (OBM) and rotational accelerations, which are typically obtained by differentiating rate gyro measurements [2]. These requirements make INDI vulnerable to inertial measurement unit (IMU) and actuator failures, potentially causing performance degradation and even instability. Although INDI is inherently robust against mismatches between the actual control effectiveness and the OBM [3], in the case of large deviations caused by actuator failures, INDI no longer guarantees closed-loop stability [4].

A potential method to address model mismatch is to use parameter estimation to update the OBM in flight, known as adaptive INDI (A-INDI) [5–7]. Typically, adaptation is preceded by a state reconstruction step to determine the observable states of interest or to filter measured states, leading to the two-step method (TSM) [8]. A well-studied approach to state reconstruction in the context of flight control is to employ extended or unscented Kalman filters with nonlinear kinematic process models [9–13]. However, since IMU measurements act as inputs to the Kalman filter, faults in IMU sensors lead to drift in state estimation [14]. Similarly, IMU measurements are also required in parameter estimation to calculate angular moments [6]. Consequently, IMU faults affect both steps of the TSM, which stresses the importance of IMU fault mitigation specifically for INDI-based flight controllers and their adaptive variants.

One approach to tackling IMU faults within the Kalman filter framework is to treat them as additional states. The drawback is that this results in a large state vector, increasing the computational load. To alleviate this issue, it is possible to decompose the filter into two stages in which state estimation and fault identification are performed separately in parallel [15–19]. However, the decomposed filter is optimal only when the faults are constant [20,21]. In [22], researchers derive a modified two-stage Kalman filter capable of optimal decomposition as long as the state covariance matrix of the fault-free filter is positive semidefinite, called the optimal two-stage Kalman filter (OTSKF). An earlier study [23] proposed an extended version of the OTSKF, called the optimal two-stage extended Kalman filter (OTSEKF), to identify artificially injected IMU faults in an offline application. Following this, a recent paper [14] improved this method by incorporating higher-order sliding mode differentiators to mitigate the initial condition sensitivity of the OTSEKF, facilitating IMU fault identification through state drift differentiation. The findings indicated that this approach is feasible due to the flat nature of the process model. The present study extends this approach to propose an active fault-tolerant control system that can handle simultaneous actuator and IMU failures in flight under the effect of turbulence.

This Note provides three main contributions. First, it investigates the impact of IMU and actuator faults on conventional and A-INDI by analyzing the underlying assumptions and demonstrating the importance of IMU fault correction in the INDI framework. Second, it builds on the approaches of [6,14] to propose an active fault-tolerant control system that can effectively deal with simultaneous actuator and IMU faults in turbulent flight conditions. This is accomplished by combining an optimal two-stage extended Kalman filter with a higher-order sliding mode (OTSEKF-HOSM) differentiator and a variable forgetting factor recursive least squares (VFF-RLS) algorithm [24]. The combination solves three problems in INDI-based fault-tolerant flight control: 1) it addresses model mismatch caused by actuator faults; 2) it mitigates IMU faults that affect state estimation, degrade the linearizing INDI law, and propagate into online parameter estimation; and 3) it provides turbulence rejection through the kinematic process model used in the OTSEKF. The resulting system is termed active-adaptive INDI (AA-INDI). Lastly, it applies the proposed active fault-tolerant control system to a novel commercial flying wing concept called the FLYING V™.§ Numerical simulations demonstrate the impact of these simultaneous faults on tracking performance and compare INDI, A-INDI, and AA-INDI.

The rest of this Note is structured as follows. Section II introduces INDI-based flight control and analyzes the impact of IMU faults on INDI and A-INDI. Section III presents the AA-INDI control structure, explains the underlying methods, and discusses fault modeling. Section IV outlines the simulation model that includes aerodynamics, sensors, actuators, turbulence, and tracking signals. Section V presents all numerical simulation results and provides a discussion. Finally, Sec. VI highlights the contributions, summarizes the main findings, and identifies the limitations.

II. Problem Definition

This section introduces conventional and A-INDI, starting with a general nonlinear system. It analyzes the underlying assumptions and demonstrates the impact of simultaneous IMU and actuator faults.

Presented as Paper 2026-1743 at the 2026 AIAA SciTech Forum, Orlando, FL, January 12–16, 2026; received 31 October 2025; accepted for publication 13 February 2026; published online 9 March 2026. Copyright © 2026 by Delft University of Technology. Published by the American Institute of Aeronautics and Astronautics, Inc., with permission. All requests for copying and permission to reprint should be submitted to CCC at www.copyright.com; employ the eISSN 1533-3884 to initiate your request. See also AIAA Rights and Permissions https://aiaa.org/publications/publish-with-aiaa/rights-and-permissions/.

*Ph.D. Candidate, Control and Simulation, Faculty of Aerospace Engineering; d.atmaca@tudelft.nl (Corresponding Author).
†Associate Professor, Control and Simulation, Faculty of Aerospace Engineering; c.c.devisser@tudelft.nl.
‡Associate Professor, Control and Simulation, Faculty of Aerospace Engineering; e.vankampen@tudelft.nl.

§Flying-V is a trademark of Fortescue. The Flying-V design is owned by Fortescue (UK & NL patents pending).

Downloaded by Technische Universiteit Delft on July 21, 2026 | http://arc.aiaa.org | DOI: 10.2514/1.G009705

A. Incremental Nonlinear Dynamic Inversion

Consider a general MIMO continuous-time nonlinear system (not necessarily control-affine),

$$\dot{\boldsymbol{x}} = \boldsymbol{f}(\boldsymbol{x}, \boldsymbol{u}) \quad \text{and} \quad \boldsymbol{y} = \boldsymbol{h}(\boldsymbol{x}) \tag{1}$$

where $\boldsymbol{x} \in \mathbb{R}^l$ represents the system states, $\boldsymbol{u} \in \mathbb{R}^m$ represents system inputs, and $\boldsymbol{y} \in \mathbb{R}^n$ represents system outputs, with $\boldsymbol{f}$ and $\boldsymbol{h}$ smooth, continuous vector fields. This nonlinear system can be approximated as a linear system in the proximity of a recent time instance using a first-order Taylor series expansion [2]:

$$\dot{\boldsymbol{x}} \approx \boldsymbol{f}(\boldsymbol{x}_0, \boldsymbol{u}_0) + \left.\frac{\partial \boldsymbol{f}(\boldsymbol{x}, \boldsymbol{u})}{\partial \boldsymbol{x}}\right|_{\boldsymbol{x}=\boldsymbol{x}_0, \boldsymbol{u}=\boldsymbol{u}_0} (\boldsymbol{x} - \boldsymbol{x}_0) + \left.\frac{\partial \boldsymbol{f}(\boldsymbol{x}, \boldsymbol{u})}{\partial \boldsymbol{u}}\right|_{\boldsymbol{x}=\boldsymbol{x}_0, \boldsymbol{u}=\boldsymbol{u}_0} (\boldsymbol{u} - \boldsymbol{u}_0) \tag{2}$$

$$\dot{\boldsymbol{x}} \approx \dot{\boldsymbol{x}}_0 + \mathbf{F}(\boldsymbol{x}_0, \boldsymbol{u}_0)(\boldsymbol{x} - \boldsymbol{x}_0) + \mathbf{G}(\boldsymbol{x}_0, \boldsymbol{u}_0)(\boldsymbol{u} - \boldsymbol{u}_0) \tag{3}$$

It is possible to simplify this expression using the time-scale separation principle. Assuming that the control actuators are sufficiently fast, $\boldsymbol{x} \approx \boldsymbol{x}_0$ at each time instance, meaning that the states are static from the perspective of fast-moving actuators. Although it is difficult to generalize the required actuator speed, a common choice is 5–10 times the system bandwidth [25]. Therefore, applying this leads to

$$\dot{\boldsymbol{x}} \approx \dot{\boldsymbol{x}}_0 + \mathbf{G}(\boldsymbol{x}_0, \boldsymbol{u}_0)(\boldsymbol{u} - \boldsymbol{u}_0) \tag{4}$$

$$\Delta \boldsymbol{u} = \mathbf{G}^{-1}(\boldsymbol{x}_0, \boldsymbol{u}_0)(\boldsymbol{\nu} - \dot{\boldsymbol{x}}_0) \tag{5}$$

where $\Delta \boldsymbol{u} = \boldsymbol{u} - \boldsymbol{u}_0$ and $\boldsymbol{\nu} = \dot{\boldsymbol{x}}$ is called the virtual control. This formulation assumes that $\dot{\boldsymbol{x}}_0$ is directly measurable or observable.

Now, consider an aircraft rotational rate control problem where $\boldsymbol{x} = \boldsymbol{\omega}$, $\boldsymbol{u} = \boldsymbol{\delta}$, $\boldsymbol{\nu} = \dot{\boldsymbol{\omega}}$, and $\boldsymbol{y} = \boldsymbol{x}$. In other words, the states are aircraft rotational rates expressed in the body-fixed frame, the inputs are control surface deflections, and the virtual controls are rotational accelerations. Rotational rates and accelerations are measurable or observable. Therefore, the linearizing law for this problem is

$$\Delta \boldsymbol{\delta} = \mathbf{M}_{\delta}^{-1}(\boldsymbol{\omega}_0, \boldsymbol{\delta}_0)(\boldsymbol{\nu} - \dot{\boldsymbol{\omega}}_0) \tag{6}$$

where $\mathbf{M}_{\delta}$ represents the control moments generated by the surfaces. Based on [1], it is possible to expand the moments and rewrite as

$$\mathbf{M}_{\delta} = \frac{\partial}{\partial \boldsymbol{\delta}}(\mathbf{J}^{-1}\mathbf{M}_{\delta}) = \mathbf{J}^{-1}\mathbf{B}_{\delta} \tag{7}$$

where $\mathbf{J}$ is the moment of inertia matrix of the aircraft, and $\mathbf{B}_{\delta}$ contains the control moment derivatives with respect to each surface, also called the control effectiveness matrix (CEM). Assuming a generic aircraft with a single elevator, aileron, and rudder possessing linear control derivatives, the CEM can be written as

$$\mathbf{B}_{\delta} = \frac{1}{2}\rho V^2 S \begin{bmatrix} bC_{l,\delta_a} & 0 & bC_{l,\delta_r} \\ 0 & \bar{c}C_{m,\delta_e} & 0 \\ bC_{n,\delta_a} & 0 & bC_{n,\delta_r} \end{bmatrix} \tag{8}$$

where ρ is the local air density, V true airspeed, S wing surface area, b wing span, and $\bar{c}$ mean aerodynamic chord. C_l, C_m, and C_n represent nondimensional roll, pitch, and yaw moment coefficients, with δ_a, δ_e, and δ_r aileron, elevator, and rudder deflections. Inserting this into Eq. (6) yields the final INDI law as

$$\begin{aligned} \Delta \boldsymbol{\delta} &= \begin{bmatrix} bC_{l,\delta_a} & 0 & bC_{l,\delta_r} \\ 0 & \bar{c}C_{m,\delta_e} & 0 \\ bC_{n,\delta_a} & 0 & bC_{n,\delta_r} \end{bmatrix}^{-1} \left(\frac{2\mathbf{J}}{\rho V^2 S}\right)(\boldsymbol{\nu} - \dot{\boldsymbol{\omega}}_0) \\ &= \mathbf{B}_{\delta,c}^{-1}\left(\frac{2\mathbf{J}}{\rho V^2 S}\right)(\boldsymbol{\nu} - \dot{\boldsymbol{\omega}}_0) \end{aligned} \tag{9}$$

where $\dot{\boldsymbol{\omega}}_0$ is obtained by differentiating the rate gyro measurements. This final expression dictates that, at each time instance, the difference between the desired and current angular moments is proportional to an incremental change in control deflections through the CEM. The total control is obtained by adding the incremental change to the previous deflection as $\boldsymbol{\delta}(t_k) = \boldsymbol{\delta}(t_{k-1}) + \Delta\boldsymbol{\delta}$. In reality, the control derivatives contained in the CEM are stored onboard the aircraft. This onboard model is utilized to calculate incremental deflections.

1. Impact of IMU and Actuator Faults on INDI

Reflecting on the derivation that led to the complete INDI law in Eq. (9), it is possible to specify three core assumptions.

Assumption 1: The control actuators must be sufficiently fast (5–10 times the system bandwidth) such that $\dot{\boldsymbol{\omega}} \approx \dot{\boldsymbol{\omega}}_0$.

Assumption 2: $\dot{\boldsymbol{\omega}}_0$ is either directly measurable or observable through other states.

Assumption 3: The onboard control effectiveness model is sufficiently accurate in representing the actual control effectiveness of the aircraft such that $\mathbf{B}_{\delta,c} \approx \mathbf{B}_{\text{act}}$.

Satisfying Assumption 1 requires reasonably fast actuators. By extension, this also implies that the actuators must remain operational during flight, which can be invalidated by actuator failures. Recall Eq. (3): if the actuators are slow, time-scale separation cannot be applied, leading to

$$\Delta \boldsymbol{u} = \mathbf{G}^{-1}(\boldsymbol{x}_0, \boldsymbol{u}_0)\left[\boldsymbol{\nu} - \dot{\boldsymbol{x}}_0 - \mathbf{F}(\boldsymbol{x}_0, \boldsymbol{u}_0)(\boldsymbol{x} - \boldsymbol{x}_0)\right] \tag{10}$$

Then, the incremental law depends not only on control derivatives but also on stability derivatives; consequently, the OBM needs to cover the complete aerodynamic model. This negates one of the core advantages of INDI, which is its lower model dependency compared to that of its nonincremental counterpart, NDI, and other feedback linearization methods.

Since $\dot{\boldsymbol{\omega}}$ is obtained by differentiating the rate gyro measurements, Assumption 2 is valid as long as the IMU sensors do not experience faults. When measurements are corrupted with Gaussian noise and time-varying faults, this leads to $\omega_{m,k} = \omega_k + \xi_k + f_k$ at time instance k, where ω_m represents the measurement, ω is the angular rate, ξ is the measurement noise, and f is the sensor fault. Differentiating the rate gyro measurements using a first-order Euler method, with Δt being the interval between readings, yields

$$\dot{\omega}_k = \frac{(\omega_k + \xi_k + f_k) - (\omega_{k-1} + \xi_{k-1} + f_{k-1})}{\Delta t} \tag{11}$$

Evidently, in the case of constant faults, i.e., biases, $f_k \approx f_{k-1}$, meaning that these types of faults have little to no impact on $\dot{\omega}_k$. However, in the case of time-varying faults, the difference $f_k - f_{k-1}$ creates a fault residual that is amplified by the differentiation process. Considering the INDI rate control law given in Eq. (9), this leads to

$$\Delta \boldsymbol{\delta} = \mathbf{B}_{\delta,c}^{-1}\left(\frac{2\mathbf{J}}{\rho V^2 S}\right)\left[\boldsymbol{\nu} - \dot{\boldsymbol{\omega}}_0 - \dot{\boldsymbol{\xi}}_0 - \dot{\boldsymbol{f}}_0\right] \tag{12}$$

where $\dot{\boldsymbol{\omega}}_0$ denotes the angular rates. Consequently, these faults directly impact the control increment $\Delta\boldsymbol{\delta}$. This can cause drift, oscillations, and even loss of control, depending on the nature of the faults. Hence, employing IMU fault identification and correction methods is important for dealing with such faults in the context of INDI-based flight control.

Downloaded by Technische Universiteit Delft on July 21, 2026 | http://arc.aiaa.org | DOI: 10.2514/1.G009705

B. Adaptive Incremental Nonlinear Dynamic Inversion

The principle of A-INDI is the in-flight estimation of the control derivatives that constitute the OBM. This is done by calculating angular moments using sensor data and recursively fitting a polynomial model to these moments through least squares, ensuring that Assumption 3 is satisfied. For a symmetric aircraft, it is possible to estimate the angular moments as follows:

$$\hat{L} = I_{xx}\dot{p}_c - (I_{yy} - I_{zz})q_m r_m - I_{xz}(\dot{r}_c + p_m q_m) \tag{13}$$

$$\hat{M} = I_{yy}\dot{q}_c - (I_{zz} - I_{xx})r_m p_m - I_{zx}(r_m^2 - p_m^2) \tag{14}$$

$$\hat{N} = I_{zz}\dot{r}_c - (I_{xx} - I_{yy})p_m q_m - I_{zx}(\dot{p}_c - q_m r_m) \tag{15}$$

p_m, q_m, and r_m are the rate gyro measurements, whereas $\dot{p}_c$, $\dot{q}_c$, and $\dot{r}_c$ are the rotational accelerations calculated by differentiation. By adhering to the same dimensionalization as in Eq. (8), these moments can be expressed in a nondimensional form as

$$\hat{C}_l = \frac{\hat{L}}{\bar{\rho}Sb}, \quad \hat{C}_m = \frac{\hat{M}}{\bar{\rho}S\bar{c}}, \quad \hat{C}_n = \frac{\hat{N}}{\bar{\rho}Sb} \tag{16}$$

where $\bar{\rho}$ is the dynamic pressure. Assume that C_l, C_m, and C_n are also available from an aerodynamic model. In practice, this aerodynamic model is essentially an informed guess based on the available data preflight. It is possible to take the difference between these two sets of angular moment expressions to generate moment residuals. For example, for the rolling moment, $\varepsilon_l = C_l - \hat{C}_l$. These moment residuals can be used in a recursive least-squares algorithm to identify elements of the control effectiveness matrix, $\hat{\mathbf{B}}_{\delta,c}$, during flight, as detailed in Sec. III.B.

1. *Impact of IMU Faults on A-INDI*

Referring to Eqs. (13–15), it is evident that using A-INDI to handle model mismatches requires IMU measurements, making it susceptible to IMU faults similar to INDI. Faults contained in rate gyro measurements p_m, q_m, and r_m affect the estimated moments $\hat{L}$, $\hat{M}$, and $\hat{N}$, as well as the rotational accelerations $\dot{p}_c$, $\dot{q}_c$, and $\dot{r}_c$. This, in turn, influences the moment residual ε, leading to inaccuracies in control effectiveness estimation. Therefore, IMU faults affect not only the linearization law but also the adaptation process that is used to tackle actuator faults in INDI-based control.

III. Active-Adaptive INDI Formulation

This section introduces the AA-INDI framework, which consists of two main steps. The first step jointly tackles state estimation and IMU fault correction while rejecting turbulence. This is followed by a fault-corrected A-INDI step, where the estimated states, angular accelerations, and corrected IMU measurements are used to calculate angular moments. These moments are utilized in a variable forgetting factor recursive least-squares algorithm to estimate and update the OBM online. Figure 1 gives a global overview of this structure. The actuator faults affect both the actuators and the aircraft aerodynamics, as explained in Sec. IV.A, while the IMU faults affect only the sensors.

A. State Estimation and IMU Fault Identification

In aircraft control, the standard method for state estimation/reconstruction is to use Kalman filters, which require prediction and measurement models. This study utilizes a nonexact aircraft kinematic model for state prediction based on ground speed measurements to facilitate turbulence rejection. The model accepts IMU measurements as inputs, which are corrupted by noise and time-varying faults.

1. *Nonexact Aircraft Kinematic Model*

Consider a general nonlinear system characterizing an aircraft kinematic model,

$$\dot{\boldsymbol{x}} \approx \boldsymbol{f}(\boldsymbol{x}(t), \boldsymbol{u}_m(t), t) + \mathbf{G}(\boldsymbol{x}(t))\boldsymbol{\xi}(t) \tag{17}$$

$$\boldsymbol{y}_m(t) = \boldsymbol{h}(\boldsymbol{x}(t), \boldsymbol{u}_m(t), t) + \boldsymbol{n}(t) \tag{18}$$

where $\boldsymbol{x}$ represents the system states, $\boldsymbol{u}_m$ is the measured system input, $\mathbf{G}$ is the noise distribution matrix, $\boldsymbol{y}_m$ denotes the measured system output, $\boldsymbol{h}$ is the measurement model, and $\boldsymbol{\xi}$ and $\boldsymbol{n}$ are input and measurement noise vectors, both of which are normally distributed and zero mean. Following [23], define the variables of this kinematic model as

$$\boldsymbol{x} = \begin{bmatrix} u^b_{\mathrm{GS}} & v^b_{\mathrm{GS}} & w^b_{\mathrm{GS}} & \phi & \theta & \psi \end{bmatrix}^T \tag{19}$$

$$\begin{aligned} \boldsymbol{u}_m &= \begin{bmatrix} A_{xm} & A_{ym} & A_{zm} & p_m & q_m & r_m \end{bmatrix}^T \\ &= \begin{bmatrix} A_x & A_y & A_z & p & q & r \end{bmatrix}^T + \boldsymbol{\xi} + \boldsymbol{f}^i \end{aligned} \tag{20}$$

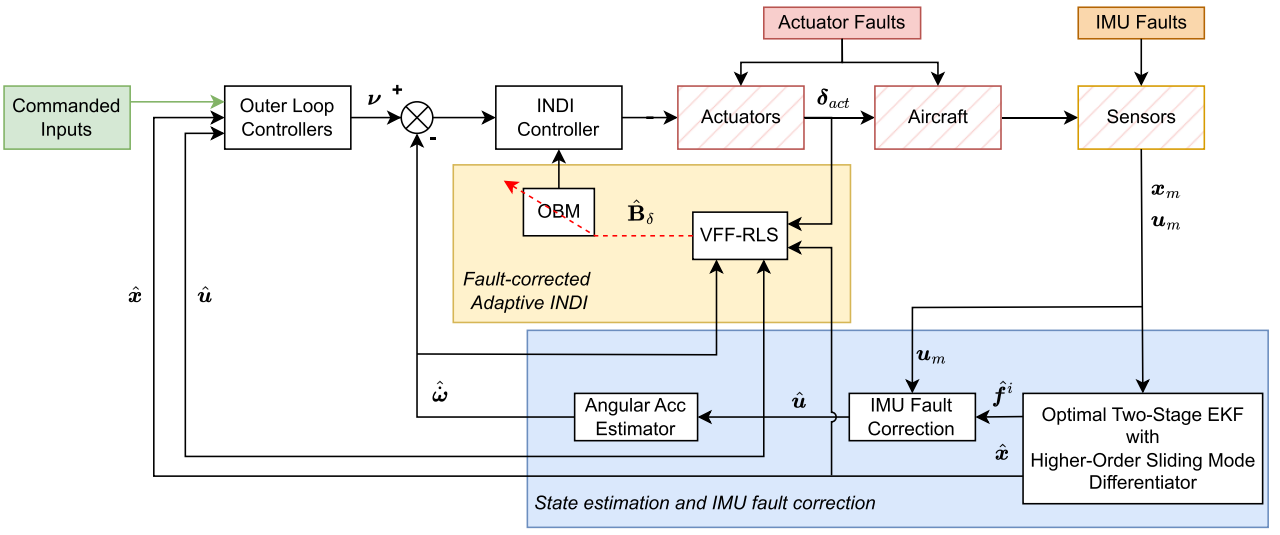

Fig. 1 Active-Adaptive INDI overview.

$$\boldsymbol{y}_m = \begin{bmatrix} u_{\mathrm{GS}_m} & v_{\mathrm{GS}_m} & w_{\mathrm{GS}_m} & \phi_m & \theta_m & \psi_m \end{bmatrix}^T = \begin{bmatrix} u_{\mathrm{GS}} & v_{\mathrm{GS}} & w_{\mathrm{GS}} & \phi & \theta & \psi \end{bmatrix}^T + \boldsymbol{n} \tag{21}$$

$$\boldsymbol{f}^i = \begin{bmatrix} f_{Ax} & f_{Ay} & f_{Az} & f_p & f_q & f_r \end{bmatrix}^T \tag{22}$$

$$\boldsymbol{\xi} = \begin{bmatrix} \xi_{A_x} & \xi_{A_y} & \xi_{A_z} & \xi_p & \xi_q & \xi_r \end{bmatrix}^T \tag{23}$$

$$\boldsymbol{n} = \begin{bmatrix} n_{u_{\mathrm{GS}}} & n_{v_{\mathrm{GS}}} & n_{w_{\mathrm{GS}}} & n_\phi & n_\theta & n_\psi \end{bmatrix}^T \tag{24}$$

where u^b_{GS}, v^b_{GS}, and w^b_{GS} are the ground speed components in the body frame; ϕ, θ, and ψ are the attitude angles; A_x, A_y, and A_z are the linear accelerations; p, q, and r are the rotational rates; and u_{GS}, v_{GS}, and w_{GS} are the ground speed components. The subscript "m" denotes the sensor-measured parameters. Therefore, the measured input $\boldsymbol{u}_m$ is expressed as the sum of the true values $\boldsymbol{u}$, IMU sensor noise $\boldsymbol{\xi}$, and true IMU faults $\boldsymbol{f}^i$. Based on these variable definitions, the process model is derived as follows [14]:

$$\dot{u}^b_{\mathrm{GS}} \approx v^b_{\mathrm{GS}}(r_m - \hat{f}_r) - w^b_{\mathrm{GS}}(q_m - \hat{f}_q) + A_{xm} - g\,\sin\theta \tag{25}$$

$$\dot{v}^b_{\mathrm{GS}} \approx -u^b_{\mathrm{GS}}(r_m - \hat{f}_r) + w^b_{\mathrm{GS}}(p_m - \hat{f}_p) + A_{ym} + g\,\cos\theta\,\sin\phi \tag{26}$$

$$\dot{w}^b_{\mathrm{GS}} \approx u^b_{\mathrm{GS}}(q_m - \hat{f}_q) - v^b_{\mathrm{GS}}(p_m - \hat{f}_p) + A_{zm} + g\,\cos\theta\,\cos\phi \tag{27}$$

$$\dot{\phi}_p \approx p_m + (q_m - \hat{f}_q)\sin\phi\,\tan\theta + (r_m - \hat{f}_r)\cos\phi\,\tan\theta \tag{28}$$

$$\dot{\theta}_p \approx q_m\cos\phi - (r_m - \hat{f}_r)\sin\phi \tag{29}$$

$$\dot{\psi}_p \approx (q_m - \hat{f}_q)\frac{\sin\phi}{\cos\theta} + r_m\frac{\cos\phi}{\cos\theta} \tag{30}$$

The nonexact nature of the model is apparent from the fault estimates, $\hat{\boldsymbol{f}}^i$. For example, in Eq. (25), since $r_m = r + \xi_r + f_r$, the total expression $(r_m - \hat{f}_r)$ becomes $r + \xi_r + f_r - \hat{f}_r$. Given that $f_r \neq \hat{f}_r$, the expression is inevitably nonexact.

The advantage of this process model is closely related to the state drift that is caused by IMU faults. Once again, focusing on Eq. (25), one may notice that, unlike the pitch and yaw rate gyro measurements, the estimated faults in A_{xm} are not subtracted from the measurement. This ensures that the drift in $\dot{u}^b_{\mathrm{GS}}$ is mainly caused by the faults in A_{xm} and not by the other IMU sensors. Consequently, it is possible to identify the fault in the IMU sensor that is measuring A_x by differentiating the drift in $\dot{u}^b_{\mathrm{GS}}$. As explained in [14], this is feasible due to the flat nature of the process model. The noise distribution matrix and the measurement model are available in [14,23] and are not given here for conciseness.

2. Optimal Two-Stage Extended Kalman Filter

In Kalman filtering, the input fault identification problem is typically addressed by considering input faults as system states. However, this results in a large state matrix, increasing computational complexity. To avoid this issue, the present study adopts the optimal two-stage formulation of [22], which has been used in the past for aircraft state and fault identification.

Following [14,23], the output of the complete filter is expressed as follows:

$$\hat{\boldsymbol{x}}_{k|k} = \bar{\boldsymbol{x}}_{k|k} + \mathbf{V}_k\hat{\boldsymbol{\mu}}^i_{k|k} \tag{31}$$

$$\mathbf{P}^{\boldsymbol{x}}_{k|k} = \mathbf{P}^{\bar{\boldsymbol{x}}}_{k|k} + \mathbf{V}_k\mathbf{P}^{\boldsymbol{\mu}^i}_{k|k}\mathbf{V}^T_k \tag{32}$$

where $\hat{\boldsymbol{x}}_{k|k}$ and $\mathbf{P}^{\boldsymbol{x}}_{k|k}$ are the final state estimates and covariance, respectively, and $\mathbf{V}_k$ is a blending matrix. These expressions are essentially a linear combination of the two filter stages, where the first and second stages take place in parallel. The first stage of the filter performs state estimation without addressing the IMU faults, allowing the states to drift. Using the notation outlined in [14,23]:

$$\bar{\boldsymbol{x}}_{k|k-1} = \bar{\boldsymbol{x}}_{k-1|k-1} + \int_{t_{k-1}}^{t_k} \boldsymbol{f}(\bar{\boldsymbol{x}}(t), \boldsymbol{u}_m(t), t)\,\mathrm{d}t + \bar{\boldsymbol{u}}_{k-1} \tag{33}$$

$$\bar{\boldsymbol{x}}_{k|k} = \bar{\boldsymbol{x}}_{k|k-1} + \boldsymbol{K}^{\bar{\boldsymbol{x}}}_k\left(\boldsymbol{y}_{m,k} - \mathbf{H}_k\bar{\boldsymbol{x}}_{k|k-1}\right) \tag{34}$$

$$\mathbf{P}^{\bar{\boldsymbol{x}}}_{k|k} = \left(\mathbf{I} - \boldsymbol{K}^{\bar{\boldsymbol{x}}}_k\mathbf{H}_k\right)\left(\boldsymbol{\Phi}_{k-1}\mathbf{P}^{\bar{\boldsymbol{x}}}_{k-1|k-1}\boldsymbol{\Phi}^T_{k-1} + \bar{\mathbf{Q}}_{k-1}\right) \tag{35}$$

$$\boldsymbol{K}^{\bar{\boldsymbol{x}}}_k = \mathbf{P}^{\bar{\boldsymbol{x}}}_{k|k-1}\mathbf{H}^T_k\left(\mathbf{H}_k\mathbf{P}^{\bar{\boldsymbol{x}}}_{k|k-1}\mathbf{H}^T_k + \mathbf{R}_k\right)^{-1} \tag{36}$$

where $\bar{\boldsymbol{x}}_{k|k-1}$ is the predicted state vector; $\boldsymbol{K}^{\bar{\boldsymbol{x}}}_k$ is the Kalman gain of the states; $\mathbf{P}^{\bar{\boldsymbol{x}}}_{k|k-1} = \boldsymbol{\Phi}_{k-1}\mathbf{P}^{\bar{\boldsymbol{x}}}_{k-1|k-1}\boldsymbol{\Phi}^T_{k-1} + \bar{\mathbf{Q}}_{k-1}$ is the covariance matrix of the predicted states; $\boldsymbol{\Phi}_{k-1}$ is the discrete system transition matrix; $\boldsymbol{\Gamma}_{k-1}$ is the discrete noise distribution matrix; and $\mathbf{F}_{k-1}$ and $\mathbf{H}_k$ are the Jacobians of the system and measurement model with respect to $\hat{\boldsymbol{x}}_{k-1|k-1}$. The discretization of the system transition and noise distribution matrices is given as follows:

$$\boldsymbol{\Phi}_{k-1} = e^{\mathbf{F}_{k-1}\Delta t} = \sum_n^\infty \frac{\mathbf{F}^n_{k-1}(\Delta t)^n}{n!}, \quad \Delta t = t_k - t_{k-1} \tag{37}$$

$$\boldsymbol{\Gamma}_{k-1} = \int_{t_{k-1}}^{t_k} \boldsymbol{\Phi}_{k-1}\mathbf{G}(\bar{\boldsymbol{x}}_{k-1|k-1})\,\mathrm{d}t \tag{38}$$

$$\mathbf{Q}_k = E\{\boldsymbol{\xi}(t)^T\boldsymbol{\xi}(t)\}, \quad \mathbf{R}_k = E\{\boldsymbol{n}(t)^T\boldsymbol{n}(t)\} \tag{39}$$

Essentially, this stage of the filter resembles the discrete formulation of an extended Kalman filter, with the exception of the coupling terms $\bar{\mathbf{Q}}_{k-1}$ and $\bar{\boldsymbol{u}}_{k-1}$. The second stage deals exclusively with estimating the drift in the state variables. Recall the kinematic model given in Eqs. (25–30). For this, the drift in the states can be expressed as

$$\hat{\boldsymbol{\mu}}^i = \begin{bmatrix} \hat{u}^b_{\mathrm{GS},d} & \hat{v}^b_{\mathrm{GS},d} & \hat{w}^b_{\mathrm{GS},d} & \hat{\phi}_d & \hat{\theta}_d & \hat{\psi}_d \end{bmatrix}^T \tag{40}$$

Drift estimation enables the recovery of states that are allowed to drift in the first stage of the filter and facilitates IMU fault identification. Based on [14,23], the equations for this stage are given as

$$\hat{\boldsymbol{\mu}}^i_{k|k} = \hat{\boldsymbol{\mu}}^i_{k|k-1} + \boldsymbol{K}^{\boldsymbol{\mu}^i}_k\left(\boldsymbol{y}_{m,k} - \mathbf{H}_k\bar{\boldsymbol{x}}_{k|k-1} - \mathbf{S}_k\hat{\boldsymbol{\mu}}^i_{k|k-1}\right) \tag{41}$$

$$\mathbf{P}^{\boldsymbol{\mu}^i}_{k|k} = \left(\mathbf{I} - \boldsymbol{K}^{\boldsymbol{\mu}^i}_k\mathbf{S}_k\right)\left(\mathbf{P}^{\boldsymbol{\mu}^i}_{k-1|k-1} + \mathbf{Q}^{\boldsymbol{\mu}^i}_{k-1}\right) \tag{42}$$

$$\boldsymbol{K}^{\boldsymbol{\mu}^i}_k = \mathbf{P}^{\boldsymbol{\mu}^i}_{k|k-1}\mathbf{S}^T_k\left(\mathbf{H}_k\mathbf{P}^{\bar{\boldsymbol{x}}}_{k|k-1}\mathbf{H}^T_k + \mathbf{R}_k + \mathbf{S}_k\mathbf{P}^{\boldsymbol{\mu}^i}_{k|k-1}\mathbf{S}^T_k\right)^{-1} \tag{43}$$

$\mathbf{P}^{\boldsymbol{\mu}^i}_{k|k-1} = \mathbf{P}^{\boldsymbol{\mu}^i}_{k-1|k-1} + \mathbf{Q}^{\boldsymbol{\mu}^i}_{k-1}$ is the fault covariance matrix, $\boldsymbol{K}^{\boldsymbol{\mu}^i}_k$ is the Kalman gain of the faults, $\mathbf{Q}^{\boldsymbol{\mu}^i}_{k-1}$ is the fault noise covariance matrix, and $\hat{\boldsymbol{\mu}}^i_{k|k-1} = \hat{\boldsymbol{\mu}}^i_{k-1|k-1}$. In addition, some auxiliary definitions are written as

$$\bar{\mathbf{U}}_k = \boldsymbol{\Phi}_{k-1}\mathbf{V}_{k-1} + \boldsymbol{\Gamma}_{k-1} \tag{44}$$

$$\mathbf{U}_k = \bar{\mathbf{U}}_k + \left(\mathbf{Q}^{\boldsymbol{x}\boldsymbol{\mu}^i}_{k+1} - \bar{\mathbf{U}}_k\mathbf{Q}^{\boldsymbol{\mu}^i}_{k-1}\right)\left(\mathbf{P}^{\boldsymbol{\mu}^i}_{k|k-1}\right)^{-1} \tag{45}$$

$$\bar{\boldsymbol{u}}_k = \left(\bar{\mathbf{U}}_{k+1} - \mathbf{U}_{k+1}\right)\hat{\boldsymbol{\mu}}^i_{k|k} \tag{46}$$

Downloaded by Technische Universiteit Delft on July 21, 2026 | http://arc.aiaa.org | DOI: 10.2514/1.G009705

$$\bar{\mathbf{Q}}_k = \mathbf{\Gamma}_k \mathbf{Q}_k \mathbf{\Gamma}_k^T - \mathbf{Q}_k^{x\mu^i} \bar{\mathbf{U}}_{k+1}^T - \mathbf{U}_{k+1}\left(\mathbf{Q}_k^{x\mu^i} - \bar{\mathbf{U}}_{k+1}\mathbf{Q}_k^{\mu^i}\right)^T \tag{47}$$

$$\mathbf{S}_k = \mathbf{H}_k \mathbf{U}_k \tag{48}$$

$$\mathbf{V}_k = \mathbf{U}_k - \boldsymbol{K}_k^{\bar{x}} \mathbf{S}_k \tag{49}$$

$\mathbf{Q}_k^{x\mu^i}$ depicts the correlation between the process and fault noise, which is equal to zero when the faults are constant.

3. Role of HOSM Differentiator

With the states and their drift estimated, the last step is identifying IMU faults. According to [14], the aircraft kinematic model employed in this study is flat, meaning that the output is related to the state and the input through differentiation and algebraic relations. This allows for the reconstruction of IMU faults by differentiating the drift in the state variables. However, since differentiation is an inherent noise amplifier, it is essential to employ a method that can attenuate noise. To this end, this study uses a discrete and nonrecursive higher-order sliding mode (HOSM) differentiator. Within the scope of this work, the HOSM offers intrinsic noise rejection capabilities and strong accuracy [26,27], while also reducing the initial condition sensitivity of the OTSEKF in identifying IMU faults [14,28]. The next section introduces A-INDI using corrected IMU measurements and angular accelerations.

B. Fault-Corrected Adaptive INDI

The second step of the AA-INDI addresses actuator faults by updating the OBM online. As introduced in Sec. II.B, this involves calculating angular moments using sensor data and recursively fitting a polynomial to estimate control derivatives, which can be performed using a VFF-RLS [24] algorithm.

1. Variable Forgetting Factor Recursive Least Squares

Assuming that IMU faults are identified in the previous step, it is possible to define a fault residual as $\boldsymbol{f}^i - \hat{\boldsymbol{f}}^i = \boldsymbol{\epsilon}_f$. For gyro measurements, this leads to $\boldsymbol{\omega}_m = \boldsymbol{\omega} + \boldsymbol{\xi} + \boldsymbol{\epsilon}_f$. Since $\boldsymbol{\epsilon}_f \ll \boldsymbol{f}^i$, this practically eliminates the impact of IMU faults on angular moment computation. Note that IMU fault identification requires several time steps to converge, during which the faults propagate into the moment residual in Eq. (53). However, since the identification is sufficiently fast, the OBM estimation is not compromised. The angular moment coefficients can then be calculated using Eq. (16). An important step in the RLS implementation is the selection of a linear polynomial model. Although using the actual aircraft structure from Eq. (58) is a natural choice for this model, this would be unrealistic since the true aircraft model is typically unknown. Therefore, based on the known control layout of the aircraft, we assume that the linear polynomial has the following form:

$$\begin{aligned} C_* = {} & C_{*_{\mathrm{LI}}}(\delta_{\mathrm{LI}}) + C_{*_{\mathrm{LO}}}(\delta_{\mathrm{LO}}) + C_{*_{\mathrm{RI}}}(\delta_{\mathrm{RI}}) + C_{*_{\mathrm{RO}}}(\delta_{\mathrm{RO}}) \\ & + C_{*_{\mathrm{Rud}}}(\delta_{\mathrm{Rud}}) \end{aligned} \tag{50}$$

where C_* represents C_l, C_m, C_n, and δ denotes the control surface deflections. The subscripts LI, LO, RI, RO, and Rud stand for left inner, left outer, right inner, right outer, and rudders, respectively, as shown in Fig. 2. Decomposing Eq. (50) leads to the following regression and parameter vectors:

$$\boldsymbol{a}_{k+1} = \begin{bmatrix} \delta_{\mathrm{LI}} & \delta_{\mathrm{LO}} & \delta_{\mathrm{RI}} & \delta_{\mathrm{RO}} & \delta_{\mathrm{Rud}} \end{bmatrix} \tag{51}$$

$$\hat{\boldsymbol{\theta}}_k = \begin{bmatrix} C_{*_{\mathrm{LI}}} & C_{*_{\mathrm{LO}}} & C_{*_{\mathrm{RI}}} & C_{*_{\mathrm{RO}}} & C_{*_{\mathrm{Rud}}} \end{bmatrix} \tag{52}$$

Following this, the moment residual for the RLS algorithm can be calculated as

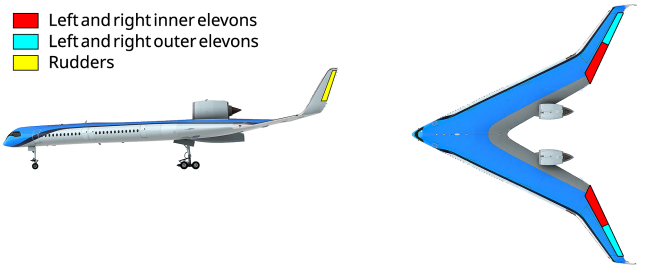

Fig. 2 Flying-V aircraft. Adapted with permission from [37]. © 2025 Delft University of Technology.

$$\boldsymbol{\epsilon}_{k+1} = y_{k+1} - \boldsymbol{a}_{k+1} \cdot \hat{\boldsymbol{\theta}}_k = \boldsymbol{y}_{k+1} - \hat{\boldsymbol{y}}_{k+1} \tag{53}$$

where $\boldsymbol{y}_{k+1}$ represents the reconstructed aerodynamic moments, $\hat{C}_l$, $\hat{C}_m$, $\hat{C}_n$, while $\hat{\boldsymbol{y}}_{k+1}$ contains the model-predicted moments. Therefore, the moment residual is defined as the difference between the reconstructed moments and those predicted by the model. The outline of the VFF-RLS algorithm is as follows [24]:

$$\boldsymbol{K}_{k+1} = \mathbf{P}_k \boldsymbol{a}_{k+1}^T \left(\boldsymbol{a}_{k+1}\mathbf{P}_k \boldsymbol{a}_{k+1}^T + 1\right)^{-1} \tag{54}$$

$$\lambda_{k+1} = \max\left\{1 - \Sigma_0^{-1}(1 - \boldsymbol{a}_{k+1}\boldsymbol{K}_{k+1})\epsilon_{k+1}^2, \lambda_{\min}\right\} \tag{55}$$

$$\hat{\boldsymbol{\theta}}_{k+1} = \hat{\boldsymbol{\theta}}_k + \boldsymbol{K}_{k+1}\boldsymbol{\epsilon}_{k+1} \tag{56}$$

$$\mathbf{P}_{k+1} = \frac{1}{\lambda_{k+1}}(\mathbf{I} - \boldsymbol{K}_{k+1}\boldsymbol{a}_{k+1})\mathbf{P}_k \tag{57}$$

where $\boldsymbol{K}_{k+1}$ is the RLS gain, $\mathbf{P}_{k+1}$ is the parameter covariance, and λ is the variable forgetting factor, with $\lambda_{\min}$ is generally set as a fixed value to ensure that the forgetting factor does not become negative or near zero, which can occur when the residual is large [29]. Σ_0 acts as a scalar tuning parameter, influencing the aggressiveness of adaptation. Typically, higher values result in slower yet more robust convergence. In this study, Σ_0 is chosen as 15, and $\lambda_{\min}$ is set to 0.25.

2. System Identification Maneuvers

In adaptive flight control design, system identification maneuvers play an important role. To facilitate timely and accurate parameter estimation, these maneuvers are used to generate information about the system of interest. To this end, this study employs separate surface excitations (SSEs) [30,31]. In this approach, all control surfaces are asynchronously excited using impulsive doublet inputs to quickly and distinctly identify the control derivatives. The SSE approach is particularly suitable for online applications due to its low implementation complexity [32]. Nevertheless, alternative approaches exist that utilize input signal optimization for parameter estimation [33,34]. To avoid destabilizing the aircraft, the excitation magnitudes are kept small and applied only in stable flight regimes, away from the flight envelope boundaries.

C. Outer-Loop Controllers

The outer guidance loops accept the C^* parameter, roll rate, and sideslip as commanded inputs. C^* is a longitudinal control law that blends load factor and pitch rate. At high speeds, the load factor component dominates, while at low speeds, pitch rate takes priority, with both contributing equally at a design-specified crossover velocity. Both the structure and the performance evaluation of these controllers are available in [35].

IV. Simulation Model and Setup

The simulation model used in this study belongs to a long-haul commercial flying wing concept called Flying-V [36,37]. This model features four elevons, two rudders, and two engines, as

Downloaded by Technische Universiteit Delft on July 21, 2026 | http://arc.aiaa.org | DOI: 10.2514/1.G009705

Downloaded by Technische Universiteit Delft on July 21, 2026 | http://arc.aiaa.org | DOI: 10.2514/1.G009705

Table 1 Sensor characteristics (adopted from [6])

Sensor	Sampling rate, Hz	Noise, σ	Unit
$u_{GS_m}, v_{GS_m}, w_{GS_m}$	10	$3.0 \cdot 10^{-2}$	m/s
V_{t_m}	100	$0.5 \cdot 10^{-2}$	m/s
α_m, β_m	100	$2.7 \cdot 10^{-4}$	rad
ϕ_m, θ_m	100	$8.7 \cdot 10^{-5}$	rad
ψ_m	100	$1.7 \cdot 10^{-4}$	rad
A_{xm}, A_{ym}, A_{zm}	100	$6.9 \cdot 10^{-4}$	m/s^2
p_m, q_m, r_m	100	$4.1 \cdot 10^{-6}$	rad/s

shown in Fig. 2. The elevons have a deflection limit of ±25 deg, while the rudders have ±30 deg. The sensor properties of this model are given in Table 1. The aerodynamic model of the aircraft has the following structure [6]:

$$C_* = C_{*_0} + C_{*_\alpha}(\alpha) + C_{*_\beta}(\beta) + C_{*_{p^*}}(p^*) + C_{*_{q^*}}(q^*) + C_{*_{r^*}}(r^*) + C_{*_{\delta_i}}(\delta_i) \tag{58}$$

where C_* represents C_l, C_m, C_n; while p^*, q^*, and r^* are nondimensional angular rates; and δ_i are control surface deflections with $i = \text{LI, LO, RI, RO, Rud}$. Further details on the control layout, engines, and aerodynamic model are available in [35].

A. Actuator Fault Modeling

Actuator faults are categorized into two types: structural damage and hardover. Control surface damage directly affects aircraft aerodynamics, while hardover represents an actuator failure with indirect but potentially more severe aerodynamic consequences. As noted in [6,38], structural damage to control surfaces results in decreased control effectiveness. Consequently, assuming that the changes in mass and center of gravity are negligible, the fault can be modeled by scaling the control effectiveness:

$$C'_{k_{\delta_i}} = C_{k_{\delta_i}} \mu_i, \quad \mu_i \in [0, 1] \tag{59}$$

where μ indicates the scaling factor, and $k = l, m, n$, and C' denotes the control derivative after the fault. Since the Flying-V model uses elevons instead of dedicated ailerons and elevators, this study focuses on elevon hardover. This type of fault has essentially two implications. First, since the surface becomes immobilized, it loses all effectiveness with respect to future control inputs. Furthermore, it generates additional moments that must be compensated for by the active surfaces. It is possible to model the change in moments caused by this as [6]

$$\Delta C_l = C_{l,e}\Delta\delta_e \qquad \Delta C_m = C_{m,e}\Delta\delta_e \qquad \Delta C_n = C_{n,e}\Delta\delta_e \tag{60}$$

where $\Delta\delta_e$ denotes the angular difference between the neutral control deflection needed to trim the aircraft and the deflection at which the surface is jammed.

B. Turbulence

All numerical simulations are online and performed under the effect of turbulence. To this end, a Dryden Turbulence Model is used to generate wind speed components in the body-fixed frame. It is important to mention that initially the wind is defined in an Earth-fixed frame, which is then transformed into the body frame via rotation matrices. This is preferred for convenience, as the simulation model uses airspeed to define the aircraft's velocity. Figure 3 gives the components of turbulence in the body-fixed frame.

C. Tracking Signals

Since the outer-loop controllers accept the C^* parameter and roll rate as inputs, the aircraft is commanded to track these simultaneously, which essentially represents a banked pull-up maneuver. Complete details on the nature of these tracking signals are available in [6].

V. Numerical Simulations and Discussion

This section presents all numerical simulation results and provides a discussion. The results are grouped into two categories. The first is simultaneous actuator and rate gyro faults, and the second is simultaneous actuator and accelerometer faults. Each group outlines the results for three different control configurations: 1) conventional INDI, 2) A-INDI, and 3) AA-INDI. The tracking results of all configurations are compared in a final subsection. All simulations follow a similar sequence in terms of fault and model update activation. Figure 4 gives an overview of the simulation timeline.

A. Simultaneous Actuator and Gyroscope Faults

The rate gyro faults occur in two time intervals, while the actuator faults start once and continue for the rest of the simulation. Tables 2 and 3 provide an overview of the faults. In both INDI and A-INDI, the two-stage filter described in Sec. III.A.2 remains operational.

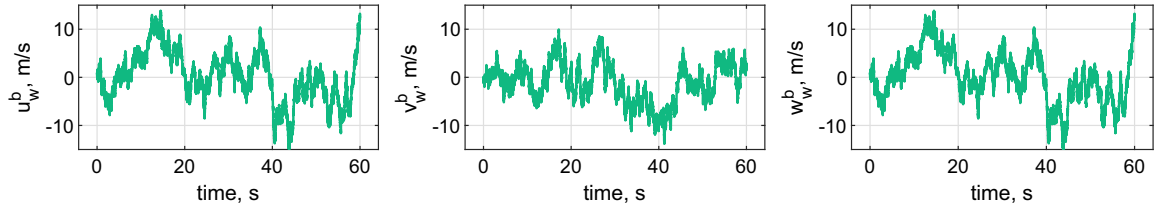

Fig. 3 Turbulent wind speed components in body frame.

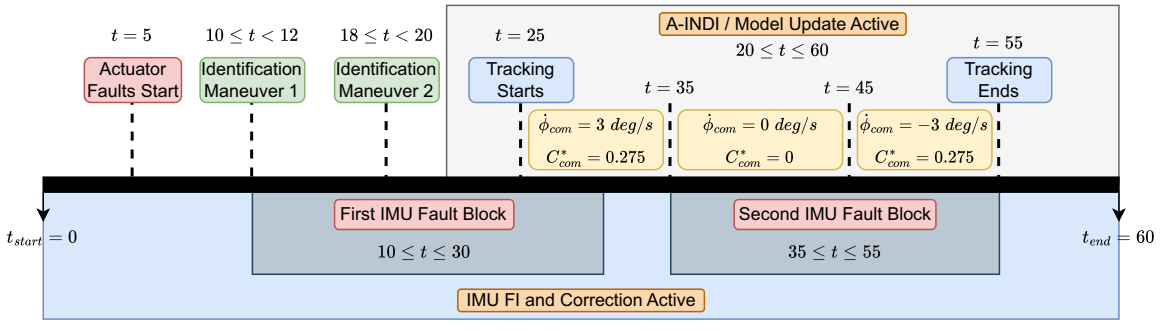

Fig. 4 Numerical simulation timeline.

Table 2 Rate gyro fault cases

Time, s	Fault	Sensor	Magnitude	Unit
	Incipient	p	$-0.125(\pi/360)(t-10)$	rad/s
$10 \le t \le 30$	Incipient	q	$1.5(\pi/360)(t-10)$	rad/s
	Step	r	$-1.5(\pi/360)$	rad/s
	Step	p	$\pi/360$	rad/s
$35 \le t \le 55$	Step	q	$2.5\pi/360$	rad/s
	Sinusoidal	r	$2\pi/180\ \sin(0.75\pi t)$	rad/s

Table 3 Actuator fault cases

Time, s	Fault	Actuator	Scaling, μ	Jammed position, deg
$t \ge 5$	Elevon hardover	Right inner elevon (RI)	0	25
$t \ge 5$	Structural loss	Left outer elevon (LO)	0.5	— —

This means that although IMU faults are not identified, any resulting drift in the state variables is corrected. Conversely, AA-INDI not only corrects state drift but also identifies and mitigates IMU faults.

1. *INDI*

This subsection presents the results for the control configuration without online CEM estimation and IMU fault identification. Figure 5 shows the control deflections and attitude angles. Starting with the control surfaces, at around 5 s, the right inner elevon (RI) quickly drifts to its deflection limit and remains immobile for the rest of the flight, which accurately represents hardover. The remaining elevons do not saturate, even though the effectiveness of the left outer elevon (LO) is halved. The rudders begin to show intermittent saturation after approximately 35 s, which aligns with the sinusoidal fault observed in the yaw rate gyro. All attitude angles exhibit some degree of oscillation. Since the command module applies a simultaneous roll rate and C^* input, a change in the attitude angles is expected. However, the consistent decrease in pitch indicates that if the simulation continues, aircraft control will likely be lost due to destabilization.

2. *Adaptive INDI*

In this configuration, the online CEM estimation is active while IMU fault correction is disabled. Figure 6 presents the control deflections and attitude angles. Although the overall trend is quite similar to the previous case, the oscillations in the attitude angles are slightly smaller. Compared to INDI, a notable difference in the control deflections is that the deflection of the left outer elevon is larger. This happens because the online CEM estimation accounts for the reduced effectiveness of this surface, informing the controller to increase the deflection to achieve the desired moment, which eliminates the need to compensate for the missing moment. Figure 7 shows the true and estimated control derivatives for the faulty surfaces. An initial transient is observed for all estimated moments, which is expected because the excitation at the beginning is insufficient for reliable parameter estimation. Once the first identification maneuver starts at 10 s, the RI estimates quickly converge to the true values, while the LO exhibits underestimation. This underestimation is likely due to insufficient excitation. The transient does not negatively impact the aircraft since the model update only starts after 20 s, allowing sufficient time for the estimates to converge. For better visibility, zoomed plots next to each figure highlight the difference between the true and estimated CEM values (note the different y-axis scale in the zoomed figures). Excluding the underestimation in the LO, the absence of IMU fault correction does not negatively affect the convergence of the estimates. The reason is that the elements of the parameter vector defined in Eq. (52) remain unaffected by IMU faults. The estimation of the control derivatives $C_{*_{\delta_i}}$ remains reliable as long as the actual control surface deflections, δ_i, are accurately measured. This is an inherent characteristic of the adopted regression model. For systems with regression models that rely on IMU measurements to identify control derivatives, IMU faults will directly impact the estimation results.

3. *Active-Adaptive INDI*

This last configuration refers to the solution proposed in this Note, where both online CEM estimation and IMU fault correction are active. Figure 8 shows the control deflections and the true attitude angles. Compared to the previous cases, the rudders do not saturate, which leaves a margin for further maneuverability. That being said, the control activity is higher, as evidenced by the small-amplitude, high-frequency oscillations observed throughout the simulation. The attitude angles also show improvement. The roll angle is visibly less oscillatory, except for three small jumps caused by the fault injection and identification maneuvers during the first 20 s. Although smaller, the yaw channel retains some fluctuations. Unlike the previous configurations, the pitch does not plummet to negative values, and it remains between 0 and 10 deg. This implies that the aircraft continues a safe flight and remains away from destabilization. The control effectiveness estimates behave similarly to those in the previous case; hence, the figure is not repeated in

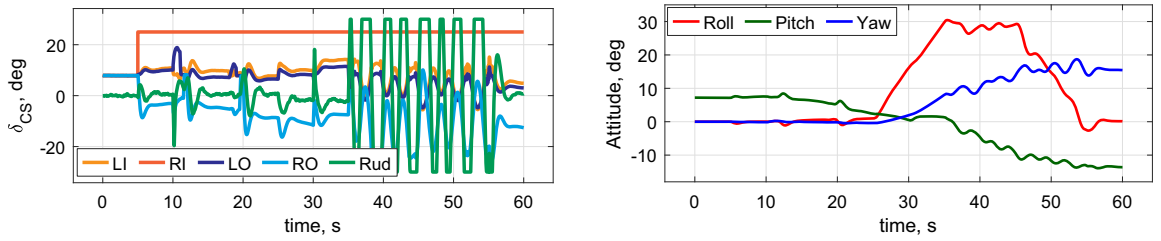

Fig. 5 Control deflections and true attitude angles for INDI.

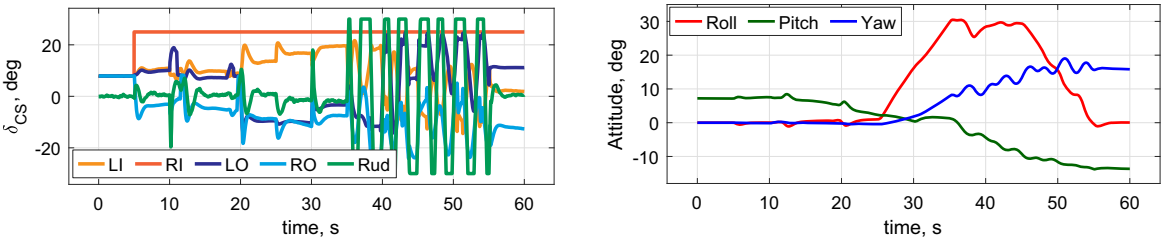

Fig. 6 Control deflections and true attitude angles for A-INDI.

Downloaded by Technische Universiteit Delft on July 21, 2026 | http://arc.aiaa.org | DOI: 10.2514/1.G009705

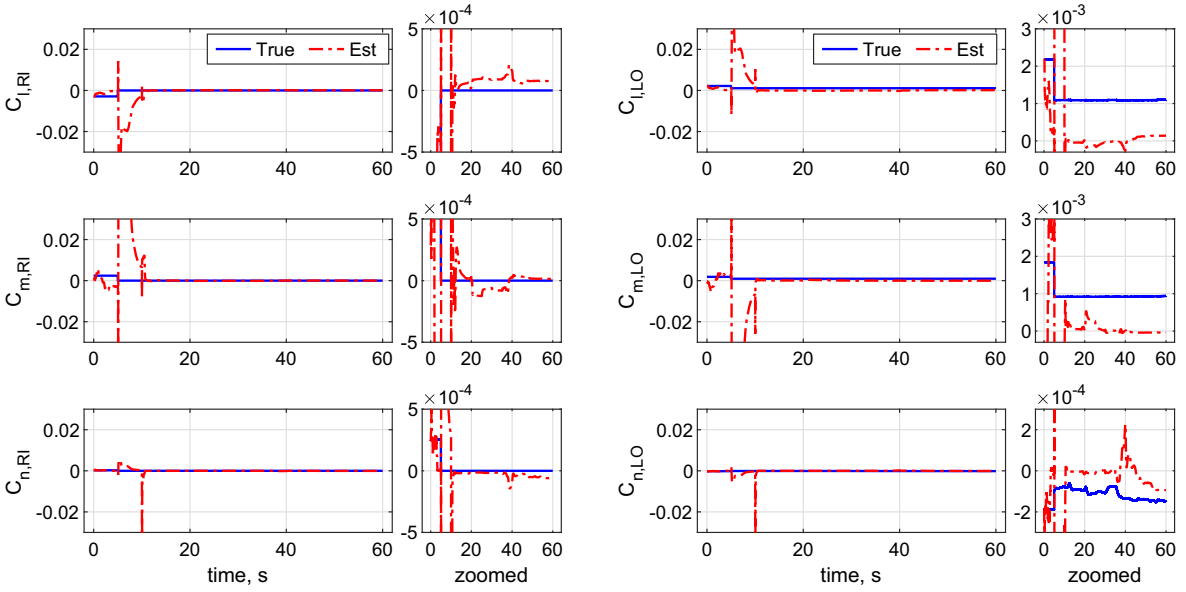

a) Right inner elevon **b) Left outer elevon**

Fig. 7 CE estimation results of faulty surfaces for A-INDI.

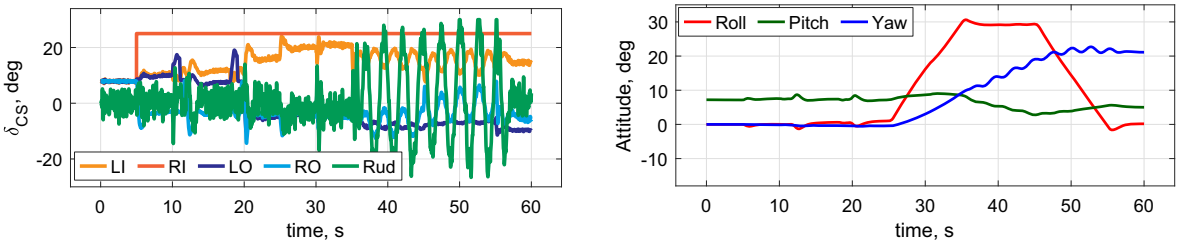

Fig. 8 Control deflections and true attitude angles with AA-INDI.

this section. Figure 9 presents the true and estimated rate gyro faults. In general, the estimates follow the time-varying faults quickly and accurately. However, for the pitch rate gyro, there are some fluctuations during the second IMU fault stage between 35 and 55 s. Recalling Eq. (29), this can be explained by the coupling between the yaw and pitch rates. Since $r_m = r + \xi_r + f_r$, the second part of the equation becomes $(r + \xi_r + f_r - \hat{f}_r)\sin\phi$. As explained in Sec. III.A.1, since fault estimation is not exact, the difference $(f_r - \hat{f}_r)$ creates a residual proportional to $\sin\phi$. Given that the roll angle is approximately 30 deg in this part of the simulation, ϵ_r is roughly calculated as $(f_r - \hat{f}_r)/2$. The residuals are present in all elements of the process model; however, they are mainly an issue for sinusoidal faults. As explained in [14], even a small time delay in fault estimation can generate a substantial sinusoidal residual. The issue can be partially resolved by increasing the sampling rate; however, this is not always possible for online applications. Lastly, Fig. 10 compares the measured, estimated, and true aircraft states used in the process model. In most cases, the state estimation follows the true values quite closely, indicating successful drift compensation. The body-frame ground speed components show minor drift, with the forward speed being the most affected. Two factors cause this phenomenon. The first is the cross-couplings of faults and imperfections in fault estimation, while the second is the low update rate of the GPS sensors. As shown in Table 1, while most sensors run at 100 Hz, the GPS operates at 10 Hz, which is a realistic characterization of GPS sensors. Although omitted here for conciseness, using the estimated states in the feedback loop instead of the measured states has a negligible impact on performance.

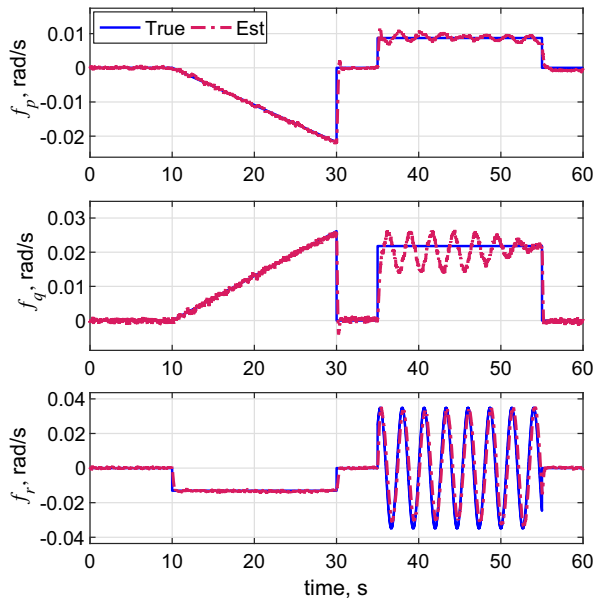

Fig. 9 True and estimated rate gyro faults.

4. *Tracking Comparison*

This section compares the tracking results of all control configurations. Figure 11 presents the roll rate and C^* tracking responses. For both signals, INDI and A-INDI show significant drift and fluctuations, failing to track the signals effectively. The performance of INDI appears to be slightly worse than that of A-INDI, with larger oscillations and transients. On the other hand, AA-INDI clearly outperforms both INDI and A-INDI, as it tracks the signals

Downloaded by Technische Universiteit Delft on July 21, 2026 | http://arc.aiaa.org | DOI: 10.2514/1.G009705

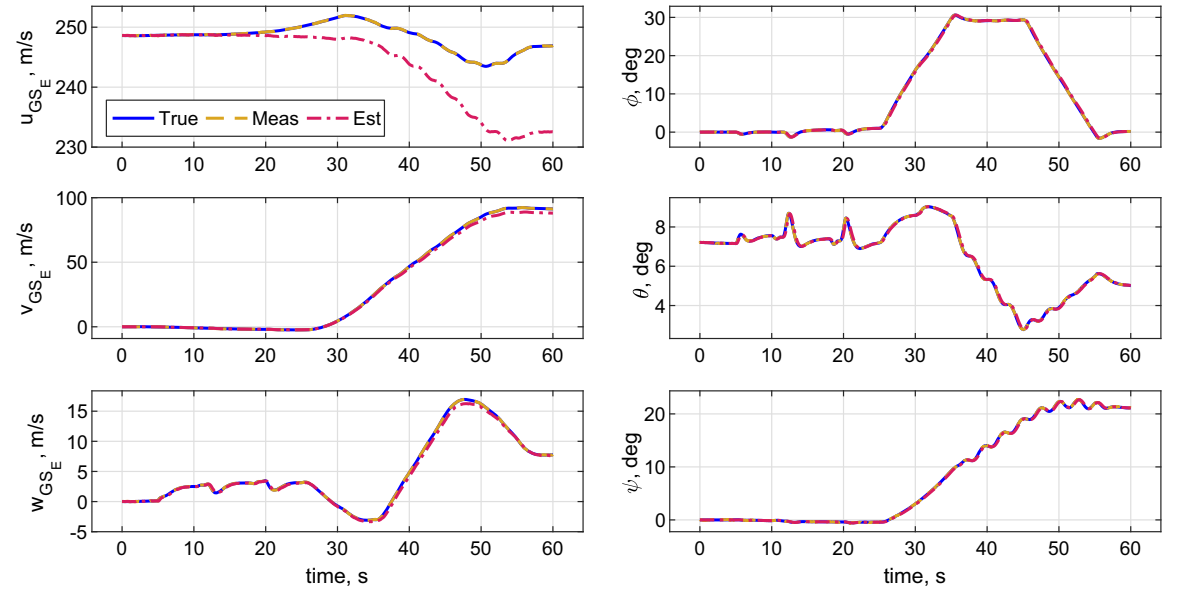

Fig. 10 Measured, estimated, and true OTSEKF states.

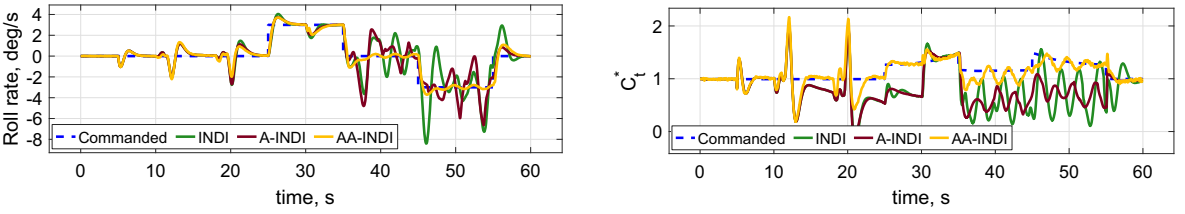

a) Roll rate tracking comparison **b) C* tracking comparison**

Fig. 11 Tracking results under gyro and actuator faults.

Table 4 RMSE comparison under gyro and actuator faults

Controller	Roll rate RMSE, deg/s	C^* RMSE
INDI	1.242	0.496
Adaptive INDI	1.033	0.454
Active-Adaptive INDI	0.580	0.199

Table 5 Accelerometer fault cases

Time, s	Fault	Sensor	Magnitude	Unit
	Step	A_x	2	m/s^2
$10 \leq t \leq 30$	Incipient	A_y	$-0.1\,(t-10)$	m/s^2
	Step	A_z	-3.75	m/s^2
	Sinusoidal	A_x	$2\sin(\pi t)$	m/s^2
$35 \leq t \leq 55$	Step	A_y	2.5	m/s^2
	Incipient	A_z	$0.1875\,(t-35)$	m/s^2

accurately without drift. Although some oscillations remain, they are much smaller in comparison. All methods show three distinct jumps during the first 20 s, which are caused by actuator fault injection at 5 s and two identification maneuvers at 10 and 18 s, as shown in Fig. 4. Table 4 provides a performance comparison using the root-mean-squared error (RMSE) between the responses and the tracking signals. Expectedly, employing AA-INDI significantly improves tracking performance compared to both INDI and A-INDI. This highlights the role of IMU fault identification and correction in simultaneously addressing IMU and actuator faults within INDI-based flight control. The improvement in RMSE provided by AA-INDI compared to INDI corresponds to 53% in roll rate and 60% in C^* tracking.

B. Simultaneous Actuator and Accelerometer Faults

This section presents simulation results with simultaneous actuator and accelerometer faults. The actuator faults match those in Table 3, while the accelerometer faults are listed in Table 5. For conciseness, this section shows only the tracking comparison. Based on Fig. 12, the roll rate responses are close for almost all control

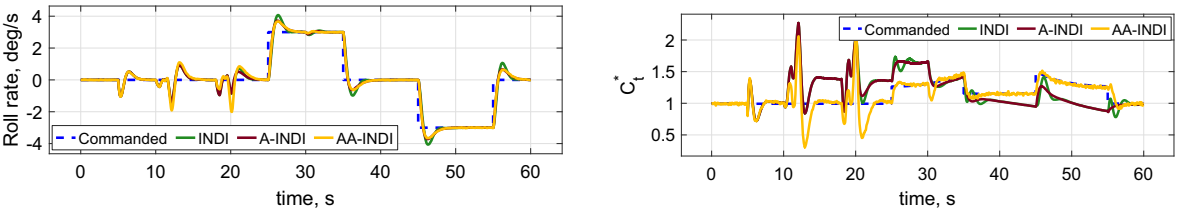

a) Roll rate tracking comparison **b) C* tracking comparison**

Fig. 12 Tracking results under accelerometer and actuator faults.

Downloaded by Technische Universiteit Delft on July 21, 2026 | http://arc.aiaa.org | DOI: 10.2514/1.G009705

Table 6 RMSE comparison under accelerometer and actuator faults

Controller	Roll rate RMSE, deg/s	C^* RMSE
INDI	0.536	0.293
Adaptive INDI	0.475	0.291
Active-Adaptive INDI	0.518	0.175

configurations, with INDI showing slightly higher overshoot. During the identification maneuvers, AA-INDI exhibits a marginally larger jump. On the other hand, in C^* tracking, both INDI and A-INDI show significant drift and large spikes. However, as expected, A-INDI is less oscillatory in transient response compared to INDI. Furthermore, AA-INDI successfully tracks the reference without drift but appears to be moderately noisier. Lastly, Table 6 provides a performance comparison using RMSE. As anticipated, the roll rate tracking results are similar, with no significant improvement in performance. In fact, AA-INDI slightly underperforms compared to A-INDI. This is likely caused by the larger jump of AA-INDI during the second identification maneuver. However, there is a clear performance improvement of 40% in C^* tracking with AA-INDI compared to INDI.

VI. Conclusions

This Note examines the impact of simultaneous IMU and actuator faults on INDI-based controllers and proposes an active fault-tolerant control system for mitigating such faults in turbulent flight conditions. The proposed AA-INDI method provides significant improvement in C^* and roll rate tracking compared to conventional and A-INDI, thanks to the two-stage Kalman filtering approach. For simultaneous rate gyro and actuator faults, AA-INDI achieves up to 53% improvement in roll rate and 60% improvement in C^* tracking compared to INDI. For simultaneous accelerometer and actuator faults, it provides 40% improvement in C^* tracking compared to INDI, with no visible improvement in roll rate. A few limitations of this method include persistent cross-couplings in the process model used in the two-stage filter and the need for both excitation maneuvers and an accurate polynomial model to facilitate control effectiveness estimation. This work demonstrates the vulnerability of INDI controllers to actuator and IMU faults and emphasizes the importance of fault-tolerant control systems for flight safety.

Acknowledgments

This publication is part of the project Flying-V Flight Control with project number 19511 of the Open Technology Program, which is partly financed by the Dutch Research Council (NWO). The authors would like to acknowledge the in-kind contributions to the project of KLM Royal Dutch Airlines and ADSE Consulting and Engineering.

References

[1] Sieberling, S., Chu, Q. P., and Mulder, J. A., "Robust Flight Control Using Incremental Nonlinear Dynamic Inversion and Angular Acceleration Prediction," *Journal of Guidance, Control, and Dynamics*, Vol. 33, No. 6, 2010, pp. 1732–1742. https://doi.org/10.2514/1.49978

[2] Bacon, B., and Ostroff, A., "Reconfigurable Flight Control Using Nonlinear Dynamic Inversion with a Special Accelerometer Implementation," *AIAA Guidance, Navigation, and Control Conference and Exhibit*, AIAA Paper 2000-4565, 2000. https://doi.org/10.2514/6.2000-4565

[3] Wang, X., van Kampen, E., Chu, Q., and Lu, P., "Stability Analysis for Incremental Nonlinear Dynamic Inversion Control," *Journal of Guidance, Control, and Dynamics*, Vol. 42, No. 5, 2019, pp. 1116–1129. https://doi.org/10.2514/1.G003791

[4] Chang, J., Breuker, R. D., and Wang, X., "Active Fault-Tolerant Incremental Sliding-Mode Flight Control Against Control Reversal," *Journal of Guidance, Control, and Dynamics*, Vol. 45, No. 12, 2022, pp. 2411–2420. https://doi.org/10.2514/1.G006690

[5] Smeur, E. J. J., Chu, Q., and de Croon, G. C. H. E., "Adaptive Incremental Nonlinear Dynamic Inversion for Attitude Control of Micro Air Vehicles," *Journal of Guidance, Control, and Dynamics*, Vol. 39, No. 3, 2016, pp. 450–461. https://doi.org/10.2514/1.G001490

[6] Atmaca, D., and van Kampen, E., "Fault Tolerant Control for the Flying-V Using Adaptive Incremental Nonlinear Dynamic Inversion," *AIAA SciTech Forum*, AIAA Paper 2025-0081, 2025. https://doi.org/10.2514/6.2025-0081

[7] Park, C., Ramirez-Serrano, A., and Bisheban, M., "Adaptive Incremental Nonlinear Dynamic Inversion Control for Aerial Manipulators," *Aerospace*, Vol. 11, No. 8, 2024, Paper 671. https://doi.org/10.3390/aerospace11080671

[8] Mulder, J. A., Chu, Q. P., Sridhar, J. K., Breeman, J. H., and Laban, M., "Non-Linear Aircraft Flight Path Reconstruction Review and New Advances," *Progress in Aerospace Sciences*, Vol. 35, No. 7, 1999, pp. 673–726. https://doi.org/10.1016/S0376-0421(99)00005-6

[9] Lombaerts, T. J., Huisman, H. O., Chu, Q. P., Mulder, J. A., and Joosten, D. A., "Nonlinear Reconfiguring Flight Control Based on Online Physical Model Identification," *Journal of Guidance, Control, and Dynamics*, Vol. 32, No. 3, 2009, pp. 727–748. https://doi.org/10.2514/1.40788

[10] Teixeira, B. O., Tôrres, L. A., Iscold, P., and Aguirre, L. A., "Flight Path Reconstruction—A Comparison of Nonlinear Kalman Filter and Smoother Algorithms," *Aerospace Science and Technology*, Vol. 15, No. 1, 2011, pp. 60–71. https://doi.org/10.1016/j.ast.2010.07.005

[11] Klein, V., and Schiess, J. R., "Compatibility Check of Measured Aircraft Responses Using Kinematic Equations and Extended Kalman Filter," NASA TN D-8514, 1977, https://ntrs.nasa.gov/citations/19770022199.

[12] He, Q., Zhang, W., Lu, P., and Liu, J., "Performance Comparison of Representative Model-Based Fault Reconstruction Algorithms for Aircraft Sensor Fault Detection and Diagnosis," *Aerospace Science and Technology*, Vol. 98, March 2020, Paper 105649. https://doi.org/10.1016/j.ast.2019.105649

[13] Youn, W., Choi, H., Cho, A., Kim, S., and Rhudy, M. B., "Accelerometer Fault-Tolerant Model-Aided State Estimation for High-Altitude Long-Endurance UAV," *IEEE Transactions on Instrumentation and Measurement*, Vol. 69, No. 10, 2020, pp. 8539–8553. https://doi.org/10.1109/TIM.2020.2988748

[14] Atmaca, D., de Visser, C., and van Kampen, E., "Online Inertial Measurement Unit Fault Identification and Active Fault-Tolerant Flight Control," *Journal of Guidance, Control, and Dynamics*, Vol. 48, No. 10, 2025, pp. 2389–2398. https://doi.org/10.2514/1.G009147

[15] Friedland, B., "Treatment of Bias in Recursive Filtering," *IEEE Transactions on Automatic Control*, Vol. 14, No. 4, 1969, pp. 359–367. https://doi.org/10.1109/TAC.1969.1099223

[16] Ignagni, M. B., "An Alternate Derivation and Extension of Friedland's Two-Stage Kalman Estimator," *IEEE Transactions on Automatic Control*, Vol. 26, No. 3, 1981, pp. 746–750. https://doi.org/10.1109/TAC.1981.1102697

[17] Mendel, J. M., "Extension of Friedland's Bias Filtering Technique to a Class of Nonlinear Systems," *IEEE Transactions on Automatic Control*, Vol. 21, No. 2, 1976, pp. 296–298. https://doi.org/10.1109/TAC.1976.1101201

[18] Zhou, D. H., Sun, Y. X., Xi, Y. G., and Zhang, Z., "Extension of Friedland's Separate-Bias Estimation to Randomly Time-Varying Bias of Nonlinear Systems," *IEEE Transactions on Automatic Control*, Vol. 38, No. 8, 1993, pp. 1270–1273. https://doi.org/10.1109/9.233167

[19] Caglayan, A. K., and Lancraft, R. E., "A Separated Bias Identification and State Estimation Algorithm for Nonlinear Systems," *Automatica*, Vol. 19, No. 5, 1983, pp. 561–570. https://doi.org/10.1016/0005-1098(83)90012-2

[20] Alouani, A., Xia, P., Rice, T. R., and Blair, W. D., "On the Optimality of Two-Stage State Estimation in the Presence of Random Bias," *IEEE Transactions on Automatic Control*, Vol. 38, No. 8, 1993, pp. 1279–1283. https://doi.org/10.1109/9.233168

[21] Keller, J. Y., and Darouach, M., "Optimal Two-Stage Kalman Filter in the Presence of Random Bias," *Automatica*, Vol. 33, No. 9, 1997, pp. 1745–1748. https://doi.org/10.1016/S0005-1098(97)00088-5

[22] Hsieh, C.-S., and Chen, F.-C., "Optimal Solution of the Two-Stage Kalman Estimator," *IEEE Transactions on Automatic Control*, Vol. 44,

Downloaded by Technische Universiteit Delft on July 21, 2026 | http://arc.aiaa.org | DOI: 10.2514/1.G009705

No. 1, 1999, pp. 194–199.
https://doi.org/10.1109/9.739135

[23] Lu, P., van Eykeren, L., van Kampen, E., de Visser, C. C., and Chu, Q. P., "Aircraft Inertial Measurement Unit Fault Identification with Application to Real Flight Data," *Journal of Guidance, Control, and Dynamics*, Vol. 38, No. 12, 2015, pp. 2467–2475.
https://doi.org/10.2514/1.G001247

[24] Fortescue, T. R., Kershenbaum, L. S., and Ydstie, B. E., "Implementation of Self-Tuning Regulators with Variable Forgetting Factors," *Automatica*, Vol. 17, No. 6, 1981, pp. 831–835.
https://doi.org/10.1016/0005-1098(81)90070-4

[25] Steffensen, R., Steinert, A., and Smeur, E. J. J., "Nonlinear Dynamic Inversion with Actuator Dynamics: An Incremental Control Perspective," *Journal of Guidance, Control, and Dynamics*, Vol. 46, No. 4, 2023, pp. 709–717.
https://doi.org/10.2514/1.G007079

[26] Levant, A., "Robust Exact Differentiation via Sliding Mode Technique," *Automatica*, Vol. 34, No. 3, 1998, pp. 379–384.
https://doi.org/10.1016/S0005-1098(97)00209-4

[27] Levant, A., and Yu, X., "Sliding-Mode-Based Differentiation and Filtering," *IEEE Transactions on Automatic Control*, Vol. 63, No. 9, 2018, pp. 3061–3067.
https://doi.org/10.1109/TAC.2018.2797218

[28] Draženović, B., "The Invariance Conditions in Variable Structure Systems," *Automatica*, Vol. 5, No. 3, 1969, pp. 287–295.
https://doi.org/10.1016/0005-1098(69)90071-5

[29] Tol, H. J., de Visser, C. C., Sun, L. G., van Kampen, E., and Chu, Q. P., "Multivariate Spline-Based Adaptive Control of High-Performance Aircraft with Aerodynamic Uncertainties," *Journal of Guidance, Control, and Dynamics*, Vol. 39, No. 4, 2016, pp. 781–800.
https://doi.org/10.2514/1.G001079

[30] Weiss, S., Friehmelt, H., Plaetschke, E., and Rohlf, D., "X-31A System Identification Using Single-Surface Excitation at High Angles of Attack," *Journal of Aircraft*, Vol. 33, No. 3, 1996, pp. 485–490.
https://doi.org/10.2514/3.46970

[31] Hamel, P. G., and Jategaonkar, R. V., "Evolution of Flight Vehicle System Identification," *Journal of Aircraft*, Vol. 33, No. 1, 1996, pp. 9–28.
https://doi.org/10.2514/3.46898

[32] Morelli, E., "In-Flight System Identification," *23rd Atmospheric Flight Mechanics Conference*, AIAA Paper 1998-4261, 1998.
https://doi.org/10.2514/6.1998-4261

[33] Klein, V., "Estimation of Aircraft Aerodynamic Parameters from Flight Data," *Progress in Aerospace Sciences*, Vol. 26, No. 1, 1989, pp. 1–77.
https://doi.org/10.1016/0376-0421(89)90002-X

[34] Morelli, E. A., "Flight Test Maneuvers for Efficient Aerodynamic Modeling," *Journal of Aircraft*, Vol. 49, No. 6, 2012, pp. 1857–1867.
https://doi.org/10.2514/1.C031699

[35] Atmaca, D., Stroosma, O., and van Kampen, E., "Piloted Evaluation of Flying-V with Incremental Nonlinear Dynamic Inversion and Envelope Protection," *AIAA SciTech Forum*, AIAA Paper 2025-0973, 2025.
https://doi.org/10.2514/6.2025-0973

[36] Benad, J., and Vos, R., "Design of a Flying V Subsonic Transport," *33rd Congress of the International Council of the Aeronautical Sciences*, ICAS Paper 2022-0358, 2022, https://www.icas.org/ICAS_ARCHIVE/ICAS2022/data/preview/ICAS2022_0358.htm.

[37] Atmaca, D., Stroosma, O., and van Kampen, E., "Design and Piloted Simulation of Envelope-Protected Control for Flying Wing Aircraft," *Journal of Guidance, Control, and Dynamics*, 2026, pp. 1–16.
https://doi.org/10.2514/1.G009479

[38] Wang, X., van Kampen, E., Chu, Q., and Lu, P., "Incremental Sliding-Mode Fault-Tolerant Flight Control," *Journal of Guidance, Control, and Dynamics*, Vol. 42, No. 2, 2019, pp. 244–259.
https://doi.org/10.2514/1.G003497

M. W. Oppenheimer
Associate Editor

Downloaded by Technische Universiteit Delft on July 21, 2026 | http://arc.aiaa.org | DOI: 10.2514/1.G009705